Shriram Swaminathan
Department of Mechanical Engineering,
The Ohio State University,
Columbus, OH 43210

N. J. Pagano
Senior Scientist Emeritus
AFRL/MLBC,
Wright-Patterson AFB, OH 45433-7750

Somnath Ghosh[1]
e-mail: ghosh.5@osu.edu
Department of Mechanical Engineering,
The Ohio State University,
Columbus, OH 43210

Analysis of Interfacial Debonding in Three-Dimensional Composite Microstructures

This paper is aimed at analyzing stresses and fiber-matrix interfacial debonding in three-dimensional composite microstructures. It incorporates a 3D cohesive zone interface model based element to simulate interfacial debonding in the commercial code ABAQUS. The validated element is used to examine the potential debonding response in the presence of fiber–fiber interactions. A two-fiber model with unidirectional fibers is constructed and the effect of relative fiber spacing and volume fraction on the stress distribution in the matrix is studied. In addition, the effect of fiber orientation and spacing on the nature of initiation and propagation of interfacial debonding is studied in a two-fiber model. These results are expected to be helpful in formulating future studies treating optimal fiber orientations and payoff in controlling fiber spacing and alignment.
[DOI: 10.1115/1.1925293]

1 Introduction

Composite materials find extensive usage in modern engineering applications. The high strength to weight ratio, coupled with favorable mechanical and thermal properties, has helped them in gaining wide commercial acceptance. The global mechanical properties of the material are affected by local failures that include particle (or fiber) splitting, interfacial debonding and matrix cracking. The occurrence of a failure mechanism depends on a number of factors like matrix, particle and interface strength, the loading mode and also on morphological parameters like fiber volume fraction, reinforcement size and shape, orientation and the spatial dispersion of the fibers in the matrix.

The fiber–matrix interface plays an important role in defining key properties of the composite like stiffness, strength and the fracture behavior. The effects of damage due to interfacial decohesion on overall mechanical properties of the composite material have been studied by various authors in [1–4]. A number of numerical models have been proposed and developed over the years to simulate the damage due to interfacial debonding in composite microstructures. One such method to simulate interfacial behavior is the cohesive zone model, where interfaces are assumed to be comprised of zero thickness nonlinear springs with a specific traction-displacement law. The approach was introduced to analyze interface failure at metal–ceramic interfaces by Needleman [5–7] and has been used by several researchers including Tvergaard [8,9], Ghosh et al. [10,11], Allen et al. [12–14], Lissenden et al. [15], Geubelle [16], and Ortiz et al. [17,18], to study damage evolution in micromechanical problems. Tvergaard [8,9] and Ghosh et al. [10,11] have used the cohesive zone model to simulate interface fracture in two-dimensional problems, while Ortiz and Pandolfi [18], Scheider [19], Segurado and LLorca [20], and Foulk et al. [12] have applied it to model failure in 3D problems. In their work, Ortiz and Pandolfi [18] have developed 3D cohesive elements with irreversible cohesive laws to simulate dynamically growing cracks and compared it with experimental results for a drop-weight dynamic fracture test. Scheider [19] has described the numerical aspects of the implementation of the cohesive model, based on the traction-separation laws developed by Needleman [5–7]. Segurado and LLorca [20] have implemented the cohesive zone model to solve the problem of decohesion in sphere-reinforced composites and Foulk et al. [12] have implemented the model to study the matrix cracking and interfacial debonding in a unidirectional metal matrix composite using a simplified two cell representative volume element (RVE). In all these models, special cohesive interface elements, defined by a constitutive equation, are created between the continuum elements. The cohesive elements open with damage initiation and lose their stiffness at failure so that the continuum elements are disconnected. Cohesive elements have been made of two quadrilateral surfaces connecting brick elements [19] or have been comprise of two triangular surfaces connecting tetrahedral elements [18,20]. These works primarily discuss the finite element aspects of the implementation of the cohesive zone for 3D microstructures to simulate interfacial debonding and validate it for specified boundary value problems. There has been limited work done in literature to address the effects of fiber spacing and orientation on the initiation and propagation of interface fracture at the microstructural level in fiber reinforced laminates.

In actual composite laminate microstructures, the fibers in two adjacent composite layers may be oriented in different directions while fibers in a single layer are susceptible to misalignment in the fabrication process. For such cases, a 2D analysis of interfacial debonding will not represent the problem accurately and the study needs to be extended to three dimensions. In order to develop a basic understanding of the phenomena of initiation and propagation of damage, this paper considers some elementary 3D problems of interacting debonding fibers and examines the influence of fiber orientation and spacing on the predicted response. Such studies may be of invaluable aid to the composite designer and fabricator, e.g., in weighing the need, or degree, of control of these parameters required in a given structure.

The problem of composite failure analysis is a complicated one. It involves multiple potential failure mechanisms as well as possible interactions between them. Thus, a useful way to evaluate failure initiation and propagation is to assume a particular mode exists by itself. This is particularly helpful when other modes have not been fully investigated and characterized. In the present case, we are concerned with matrix or interface failure. It is generally thought that the pertinent failure mechanisms involved are cavitation, shearing, and debonding of the fiber–matrix interface. Since our primary concern here is debonding, we shall offer predictions of the initiation and propagation of this mode in the absence of the

[1]Corresponding author. Suite 255, 650 Ackerman Road, The Ohio State University, Columbus, OH 43202. Tel: +1-614-292-2599; Fax: +1-614-292-3163.

Contributed by the Materials Division of ASME for publication in the JOURNAL OF ENGINEERING MATERIALS AND TECHNOLOGY. Manuscript received January 17, 2005; final manuscript received March 18, 2005. Review conducted by Greg Schoeppner. Paper presented at the 2004 ASME International Mechanical Engineering Congress (IMECE2004), November 13, 2004–November 19, 2004, Anaheim, CA, USA.

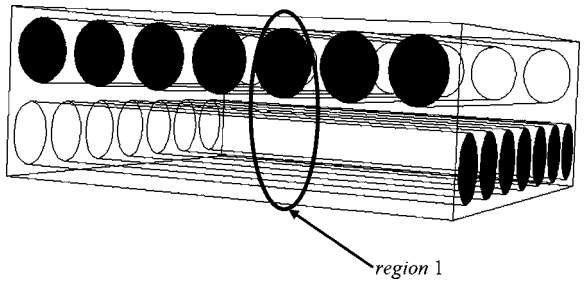

Fig. 1 A two layer composite laminate with layers aligned perpendicular with one another

other two potential failure mechanisms. This has the effect of assuming the matrix in our case is sufficiently "strong" to fully resist cavitation and shearing failure. While we neglect these modes in the analysis, we shall report the associated parameters which are assumed to control these failures, i.e., the hydrostatic stress and Von Mises stress, for the cavitation and shearing failures, respectively. Hence, once the failure parameters are given for the particular matrix being considered, one can establish whether or not the prediction of debonding is credible.

This paper implements a 3D cohesive element made up of two eight-noded quadrilateral surfaces that are compatible with the standard twenty-node brick elements using the finite element software ABAQUS [21]. The element has been developed for a small displacement formulation. The cohesive element uses the constitutive equation as defined by the bilinear model [17,18] for representing the debond crack. The element is validated by comparing the results of simulations done using ABAQUS for a 3D model with cohesive interface elements with that of the equivalent 2D simulations performed using Voronoi Cell Finite Element Model (VCFEM) [10,11,22–24] for specific 2D boundary value problems. Initially, a small region, comprising two fibers, is isolated from a composite laminate (Fig. 1) and the effect of fiber orientation and spacing on the nature of debonding initiation and progression is studied in detail on this two fiber model. Figure 1 shows a two layer composite laminate with the layers aligned perpendicular to one another. A small region with two fibers, indicated as *region 1* in Fig. 1, is isolated from the laminate and treated in the analysis. Initially, the two fibers are modeled such that, they are aligned parallel with each other [Fig. 3(*a*)]. For a prescribed boundary value problem and with a continuous interface between the fiber and matrix, the stresses in the matrix are studied as a function of relative fiber spacing and volume fraction. The study is then extended to oriented fibers (Figs. 8 and 9) and undergoing interfacial debonding. For different angles of orientation, the initiation and progression of interfacial debonding are studied for the 3D model with two fibers for specific boundary value problems. A set of metrics is used to quantify and compare the interfacial damage for various fiber orientations.

2 The Cohesive Zone Model

The cohesive zone can be used to represent debonding failure at the fiber–matrix interfaces, which are modeled as sets of nonlinear springs in the normal and tangential directions. The springs are of infinitesimal length and are attached to the fiber and the matrix at their end points. As the displacement increases, the traction across the interface reaches a maximum value, then decreases for further increase in displacement and finally vanishes indicating the failure of the spring. Needleman [7] has proposed a number of potential cohesive zone models with polynomial and exponential functions for the traction-displacement jump relation. Camacho and Ortiz [17], Ortiz and Pandolfi [18] have developed irreversible cohesive laws for the unloading path after the interfacial softening.

The relation between the traction, T, and the effective opening displacement, δ, in the cohesive zone model is given through a free energy potential ϕ as

$$T = \frac{\partial \phi(\delta_n, \delta_{t1}, \delta_{t2}, q)}{\partial \delta} \tag{1}$$

with q being a collection of internal variables to address the inelastic process of decohesion. The effective opening displacement jump, δ, in three dimensions is defined as

$$\delta = \sqrt{\delta_n^2 + \beta^2 \delta_t^2} = (u_m - u_f) \tag{2}$$

where, δ_n is the displacement jump in normal direction, $\delta_t (= \sqrt{(\delta_{t1}^2 + \delta_{t2}^2)})$ is the net displacement jump in tangential directions δ_{t1} and δ_{t2} respectively and β is an empirical factor introduced to provide a weight to the contribution of the tangential displacement jump δ_t toward the total displacement jump δ. The subscripts m and f correspond to the matrix and fiber, respectively. The normal interfacial separation $\delta_n (= u_n^m - u_n^f)$ and the tangential interfacial separations $\delta_{t1} (= u_{t1}^m - u_{t1}^f)$ and $\delta_{t2} (= u_{t2}^m - u_{t2}^f)$ are related to the interfacial traction components (T_n, T_{t1}, T_{t2}) by the cohesive laws that govern the nonlinear interfacial springs along the normal and tangential directions. The bilinear cohesive zone models have been found to satisfactorily agree with the experimentally determined macroscopic stress–strain and the load-displacement responses responses for certain composites in [11,25]. The scalar form of the normal and tangential traction-displacement relations is obtained from Eq. (1) as

$$T = \begin{cases} \dfrac{\sigma_{\max}}{\delta_c}\delta & \text{if } \delta \leqslant \delta_c \text{ (hardening region)} \\ \dfrac{\sigma_{\max}}{\delta_c - \delta_e}(\delta - \delta_e) & \text{if } \delta_c < \delta \leqslant \delta_e \text{ (softening region)} \\ 0 & \text{if } \delta > \delta_e \text{ (complete debonding)} \end{cases} \tag{3}$$

The normal and tangential tractions are consequently derived as

$$T_n = \frac{\partial \phi}{\partial \delta_n} = \frac{\partial \phi}{\partial \delta}\frac{\partial \delta}{\partial \delta_n} = \begin{cases} \dfrac{\sigma_{\max}}{\delta_c}\delta_n & \text{if } \delta \leqslant \delta_c \\ \dfrac{\sigma_{\max}}{\delta}\dfrac{\delta - \delta_e}{\delta_c - \delta_e}\delta_n & \text{if } \delta_c < \delta \leqslant \delta_e \\ 0 & \text{if } \delta > \delta_e \end{cases} \tag{4}$$

and

$$T_{ti} = \frac{\partial \phi}{\partial \delta_{ti}} = \frac{\partial \phi}{\partial \delta}\frac{\partial \delta}{\partial \delta_{ti}} = \begin{cases} \dfrac{\sigma_{\max}}{\delta_c}\beta^2\delta_{ti} & \text{if } \delta \leqslant \delta_c \\ \dfrac{\sigma_{\max}}{\delta}\dfrac{\delta - \delta_e}{\delta_c - \delta_e}\beta^2\delta_{ti} & \text{if } \delta_c < \delta \leqslant \delta_e \\ 0 & \text{if } \delta > \delta_e \end{cases} \tag{5}$$

for $i = 1, 2$

Figures 2(*a*) and 2(*b*) show the normal traction-separation response for $\delta_{t1} = \delta_{t2} = 0$ and tangential traction-separation response for $\delta_n = 0$, respectively. For a positive normal displacement, δ_n, the traction at the interface increases linearly to a maximum value of $\sigma_{\max}$ corresponding to δ_c. After that, the traction starts decreasing with increase in separation and reaches zero at a value of δ_e.

The unloading behavior in the hardening region follows the same slope as that of the loading path. In the softening region, unloading is assumed to follow a different linear path back from the current position to the origin with a reduced stiffness [line BO in Figs. 2(*a*) and 2(*b*)] and is expressed as

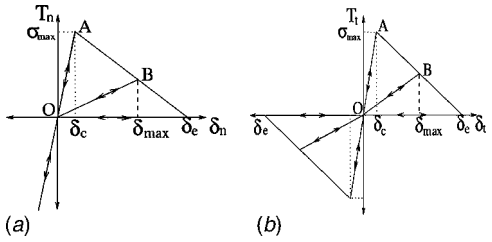

Fig. 2 (*a*) Traction displacement relation ($T_n - \delta_n$) of the bilinear cohesive zone model for normal direction with $\delta_{t1} = \delta_{t2} = 0$, (*b*) traction displacement relation ($T_t - \delta_t$) for tangential direction with $\delta_n = 0$

$$T = \frac{\sigma_{\max}}{\delta_{\max}} \frac{\delta_{\max} - \delta_e}{\delta_c - \delta_e} \quad \delta_c < \delta_{\max} < \delta_e \quad \text{and} \quad \delta < \delta_{\max} \tag{6}$$

Reloading follows the hardening slope OB and then continues along the softening slope. This demonstrates the irreversible nature of the damage process. The normal component of the traction is transferred through the normal springs, while the shear component of the traction is transferred through the tangential springs. It should be noted that both the normal and the tangential tractions vanish when $\delta \geqslant \delta_e$. Also, the magnitudes of the tangential traction-displacement relation are independent of the sign and hence, the behavior is the same for both positive and negative δ_{t1} and δ_{t2} separations. If the normal displacement is negative in compression, stiff penalty springs with high stiffness are introduced between the node-pairs at the interface to prevent penetration. From the above traction-displacement relations, it can be seen that the cohesive zone parameters ($\sigma_{\max}$, δ_c, δ_e, and β) that define the shape of the curve.

3 Cohesive Element Implementation and Validation

The cohesive model is implemented as three-dimensional cohesive elements within the FE software ABAQUS [21] using the User defined Element (UEL) subroutines [19,20]. The 3D cohesive elements have 16 nodes with a quadratic displacement formulation. These elements are written for the theory of small displacement and are compatible with the regular continuum 20 node brick elements in ABAQUS. The element is comprised of two cohesive surfaces of 8 nodes each. In the initial unloaded state, the nodes of the two surfaces share the same coordinates. With the application of external load, the surfaces move and separate from one another as the adjacent solid elements deform. The relative normal and tangential tractions for the 3D cohesive elements are calculated at the element integration points according to the traction separation law defined by the bilinear model. The element has nine integration points corresponding to that of a standard QUAD-8 element. Figure 3(*a*) shows a two fiber 3D composite model with the cohesive elements at the interface. The interface element with the two cohesive surfaces is shown in Fig. 3(*b*). The two surfaces share the same coordinates initially, but have been plotted with a separation for clarity. The fiber and matrix have been meshed using 20 node brick elements. Following the procedure of Segurado [20] and Scheider [19], the virtual work for a cohesive element is given by

$$\delta \prod^{\text{el}} = \int_S T \,.\, \delta[u] dS \tag{7}$$

where T is the cohesive traction acting on the separation $[\boldsymbol{u}]$ over the area dS. The interface element has 48 degrees of freedom in the global coordinate system, whose displacements at the nodes will be represented by a 48×1 column vector $\mathbf{u_e}$ as

$$u_e = (u_x^1, u_y^1, u_z^1, u_x^2, u_y^2, u_z^2, \ldots, u_x^{16}, u_y^{16}, u_z^{16})^T \tag{8}$$

The relative displacement jump between the paired nodes of the element surfaces in the global coordinate system will be given by a column vector, δu_e as

$$\overset{24\times1}{\{\delta u_e\}} = \overset{24\times48}{[\Phi^1]} \begin{Bmatrix} u_e^+ \\ u_e^- \end{Bmatrix} = \overset{24\times24\ \ 24\times24}{[\ [I]\ ,[-I]]} \begin{Bmatrix} u_e^+ \\ u_e^- \end{Bmatrix} \tag{9}$$

The $[\Phi^1]$ matrix comprises of two identity matrices $[I_{24\times24}]$ and $[-I_{24\times24}]$ to compute the displacement jump between the paired node sets $\{u_e^+\}$ and $\{u_e^-\}$ on opposite sides of the cohesive springs. The $\{u_e^+\}$ corresponds to the displacement components of the cohesive surface consisting of nodes 9–16, as shown in Fig. 3(*b*), while $\{u_e^-\}$ denotes the degrees of freedom for the other surface comprising of nodes 1–8. A local coordinate system for the cohesive element is defined using the natural element coordinates ξ

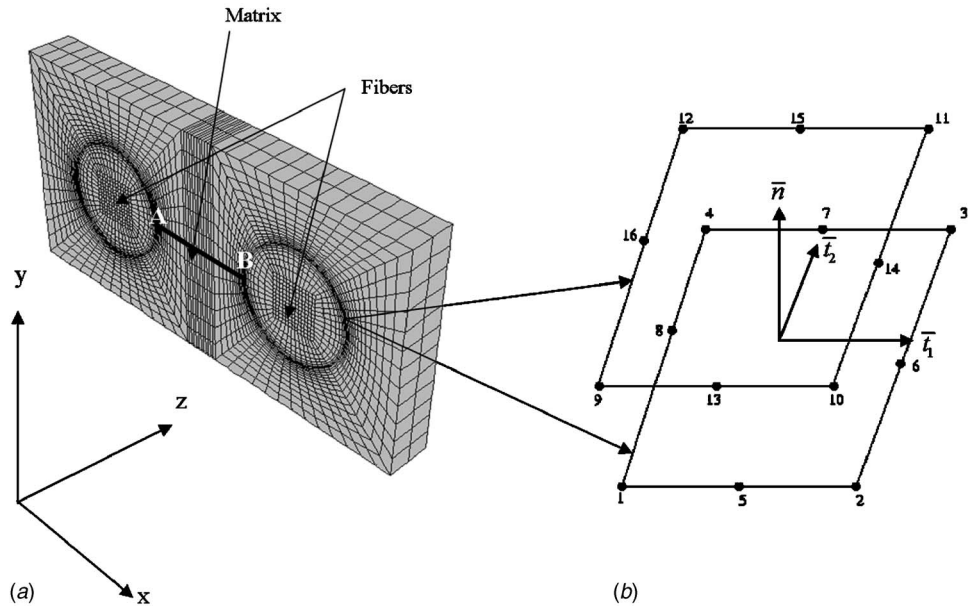

Fig. 3 (*a*) 3D model of a two-fiber model with parallel fibers (*b*) cohesive interface finite element surfaces with the local coordinate system

and η with $0 \leqslant \xi \leqslant 1, 0 \leqslant \eta \leqslant 1$. The shape function for the node pair is then given by $\varphi_i(\xi, \eta)$ $(i=1,8)$. The relative displacement jump between the element faces at any point (ξ, η) can be interpolated as a function of the relative displacement jump between paired nodes as

$$\Delta u(\xi, \eta) = \begin{pmatrix} \Delta u_x(\xi, \eta) \\ \Delta u_y(\xi, \eta) \\ \Delta u_z(\xi, \eta) \end{pmatrix} = \Phi^2(\xi, \eta) \Delta u_e \tag{10}$$

where Φ^2 is 3×24 matrix given as

$$\Phi^2(\xi, \eta) = (\varphi_1 I_{3\times3} | \varphi_2 I_{3\times3} | \cdots | \varphi_7 I_{3\times3} | \varphi_8 I_{3\times3}) \tag{11}$$

Equations (10) and (9) result in

$$\Delta u(\xi, \eta) = \Phi^2 \Phi^1 u_e = \Phi u_e \tag{12}$$

where Φ is the 3×48 matrix to compute the relative opening at any point in the element. The current normal and tangential directions are computed in the local coordinate system with the coordinates ξ and η. Since the element is for the theory of small displacement, the reference surface for the coordinate system is defined by the 8 nodes of the cohesive surface that are part of the fiber. If the global coordinates of the 8 nodes that constitute the reference surface, $x_e(x, y, z)$ are represented by a 24×1 vector, the coordinates of a point in the reference surface, $x_L(\xi, \eta)$ in the local coordinate system can be obtained as

$$x_L(\xi, \eta) = \Phi^2(\xi, \eta) x_e \tag{13}$$

The local coordinate system in the current configuration can be obtained from the three perpendicular vectors, $\bar{n}, \bar{t}_1, \bar{t}_2$ [Fig. 3(*b*)] of unit modulus expressed as

$$\bar{n} = \frac{1}{\left\| \frac{\partial x_L}{\partial \xi} \times \frac{\partial x_L}{\partial \eta} \right\|} \left(\frac{\partial x_L}{\partial \xi} \times \frac{\partial x_L}{\partial \eta} \right), \quad \bar{t}_1 = \frac{1}{\left\| \frac{\partial x_L}{\partial \xi} \right\|} \left(\frac{\partial x_L}{\partial \xi} \right), \quad \bar{t}_2 = \bar{n} \times \bar{t}_1 \tag{14}$$

where $\bar{n}$ is normal to the surface and $\bar{t}_1$ and $\bar{t}_2$ are tangential to the surface. The rotation matrix, R to transform the global coordinate system (x, y, and z) to the local coordinate system (ξ and η) is a 3×3 matrix given by

$$R = \begin{pmatrix} \bar{n}^T \\ \bar{t}_1^T \\ \bar{t}_2^T \end{pmatrix} \tag{15}$$

The tangent stiffness matrix and the force vector of the interface element can now be expressed in terms of the global coordinate system. The global tangent stiffness for the interface element in this case will be of the form of a 48×48 matrix given by

$$K^{\text{el}} = \int_{-1}^{1} \int_{-1}^{1} \Phi^T R^T \frac{\partial T_{\text{loc}}}{\partial \Delta u_{\text{loc}}} R \Phi J d\xi d\eta \tag{16}$$

where K^{el} is the element stiffness matrix in global coordinates. T_{loc} stands for the 3×1 vector that provides the normal and tangential tractions (T_n, T_{t1}, T_{t2}), given by Eqs. (4) and (5), in the current local coordinates while $\boldsymbol{u}_{\text{loc}}$ is a 3×1 vector that gives the relative displacement between the cohesive surfaces $(\delta_n, \delta_{t1}, \delta_{t2})$ in the current local coordinates. J is the Jacobian of the transformation between the local coordinates (ξ and η) and the global coordinates (x, y, and z) for the current configuration. The nodal forces for the interface element will be given by a 48×1 vector represented as

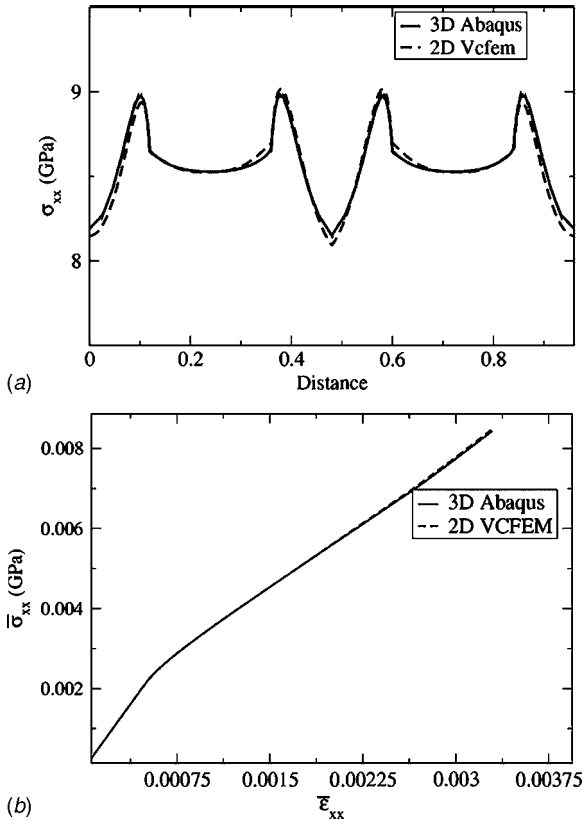

Fig. 4 Comparison of 3D Abaqus model and 2D VCFEM model for (*a*) σ_{xx} distribution along the length of the two-fiber model; (*b*) macroscopic stress–strain ($\bar{\varepsilon}_{xx}$–$\bar{\sigma}_{xx}$) plots for applied uniaxial displacement corresponding to $\bar{\varepsilon}_{xx}$=3.2e−03

$$f^{\text{el}} = \int_{-1}^{1} \int_{-1}^{1} \Phi^T R^T T_{\text{loc}} J d\xi d\eta \tag{17}$$

The UEL is written as an external subroutine and is invoked by ABAQUS to obtain the stiffness matrix and force matrix for the interface elements. The parameters associated with the cohesive element definition in ABAQUS are the number of nodes for the element and their connectivity, the cohesive zone parameters associated with the element and the solution dependent state variables required for the element.

Validation of the interface cohesive element is done by comparing the results of the 3D ABAQUS models with the equivalent 2D VCFEM model, developed by Ghosh et al. [10,11,22–24] to analyze large microstructural regions with arbitrary dispersions, shapes and sizes of heterogeneities, as in micrographs of composite materials, using an assumed stress hybrid finite element formulation. A composite microstructural model consisting of two circular fibers with equal radii r of 1.75 μm is modeled in 3D using ABAQUS in such a way that the fibers are parallel with one another and aligned along the z direction as shown in Fig. 3(*a*). The length and width of the model are constructed to be 14 and 7 μm, respectively while the thickness of the model is assigned a value of 1.5 μm. The matrix material is epoxy with Young's modulus, E=3.67126 GPa and Poisson's ratio, υ=0.328 while the fiber material is steel with E=210 GPa and υ=0.3. The same constituent elastic moduli are used throughout this paper. A corresponding two fiber model with the same dimensions and material properties is modeled in two dimensions for VCFEM analysis. Plane strain boundary conditions with ε_{zz}=0 is imposed for both the 3D and the 2D models. The FEA model is constrained so that the bottom face and the left face are constrained in the y-direction

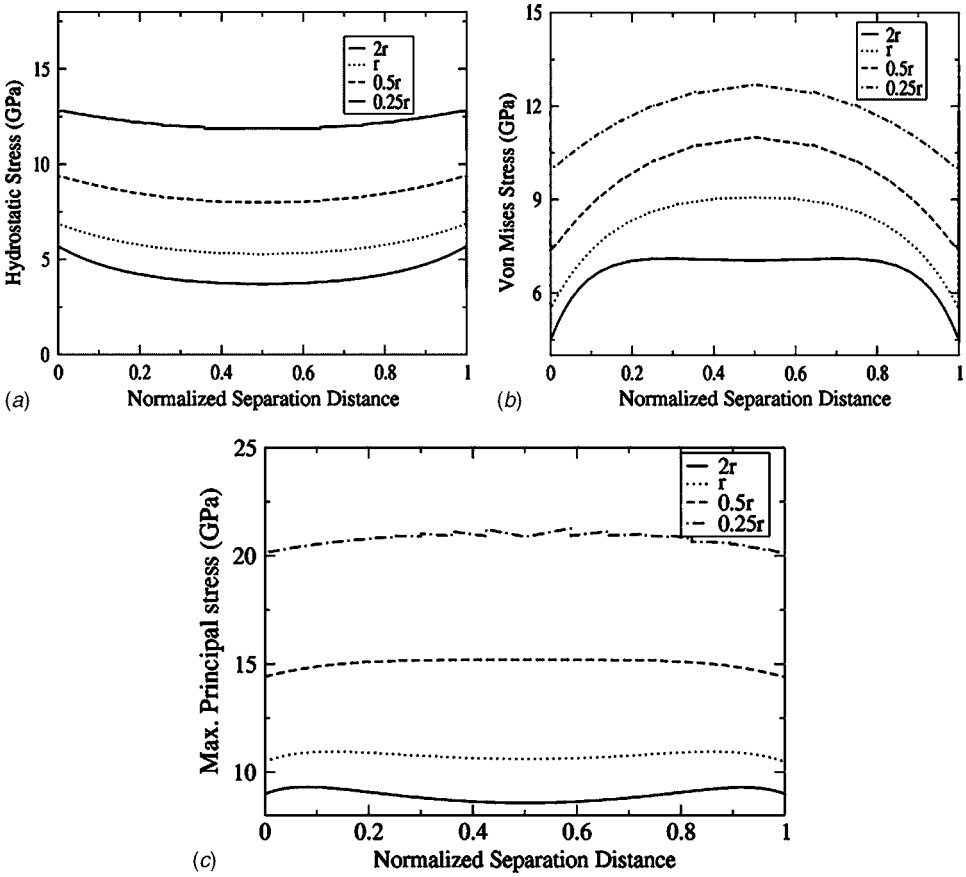

Fig. 5 Effect of fiber separation on the distribution of (*a*) hydrostatic stress; (*b*) Von Mises stress; and (*c*) maximum principal stress for an applied uniaxial displacement corresponding to $\bar{\varepsilon}_{xx}=1$ and for a fiber radii, $r=1.75\ \mu$m

and x-direction, respectively. Periodic boundary conditions are imposed on the top face such that the face remains straight and all the nodes lying on the face have equal displacement in the y-direction. Equivalent boundary conditions are prescribed on the edges of the corresponding 2D VCFEM model.

The 3D model is initially validated for continuous interfaces meaning that there is no damage due to interfacial debonding in the microstructure. This is achieved by specifying a high value ($\approx 10^6$) for the peak stress value, $\sigma_{\max}$ in the bilinear model resulting in a very steep slope for hardening. A uniaxial displacement corresponding to $\bar{\varepsilon}_{xx}=1$ is applied along the positive x-direction for both the 3D and 2D models. The distribution of the various stress components are compared for the 3D and 2D models and are found to exhibit the same values for both the cases. Figure 4(*a*) shows the comparison of the values of σ_{xx} plotted along a line drawn through the length of the model passing though the center of the fibers for the 3D ABAQUS model and the 2D VCFEM model. It is observed from Fig. 4(*a*) that both the models have matching plots for the stress distribution. The model is also checked for applied biaxial displacements in the x and y-directions and the results for the 3D model are found to match satisfactorily with the 2D model.

The 3D model is next applied for the two-fiber model with an interface defined by the bilinear cohesive law. For the previously defined matrix and fiber material properties, the cohesive interface parameters are assigned to the interface elements for both the 3D and 2D models and compared for prescribed boundary value problems. The parameters for the cohesive zone law for the interface elements are maximum stress, $\sigma_{\max}=0.0025$ GPa, critical displacement jump $\delta_c=5.1\times10^{-5}$, displacement jump for failure $\delta_e=6.2\times10^{-4}$ and the weight for the tangential displacement jump $\beta=0.707$. For the FEA boundary conditions described previously, a uniaxial displacement corresponding to $\bar{\varepsilon}_{xx}=3.2\text{e}-03$ is applied in the positive x-direction to the 3D ABAQUS and 2D VCFEM models. The comparison of the macroscopic stress strain ($\bar{\varepsilon}_{xx}-\bar{\sigma}_{xx}$) plots for the 3D and the 2D models have been depicted in Fig. 4(*b*). The macroscopic stresses and strains are obtained by volume averaging of the microscopic stresses and strains. The macroscopic stress $\bar{\sigma}_{ij}$ is the volume averaged stress obtained by integrating the stress over the microstructural model [26,27] as

$$\bar{\sigma}_{ij}=\frac{1}{Y}\int_Y \sigma_{ij}(Y)dY \tag{18}$$

The corresponding macroscopic strain $\bar{\varepsilon}_{ij}$ is the volume averaged strain, expressed as

$$\bar{\varepsilon}_{ij}=\frac{1}{Y}\int_Y \varepsilon_{ij}(Y)dY+\frac{1}{2Y}\int_{\partial Y_{\text{int}}}([u_i]n_j+[u_j]n_i)dS \tag{19}$$

Here $[u_i]$ denotes the jump of the displacement components across the interface with an outward normal n_i. The interface Y_{int} is expressed as a region between the matrix and inclusion boundaries. It can be inferred from Fig. 4(*b*) that both the 2D and 3D models exhibit equivalent $\bar{\varepsilon}_{xx}-\bar{\sigma}_{xx}$ distribution. Within a small error, the stress distribution pattern observed for the 3D and 2D models for all the components of stresses along with the extent of damage are found to be the same. A similar study is also done for a biaxial case where displacements corresponding to $\bar{\varepsilon}_{xx}=3.2\text{e}-03$ and

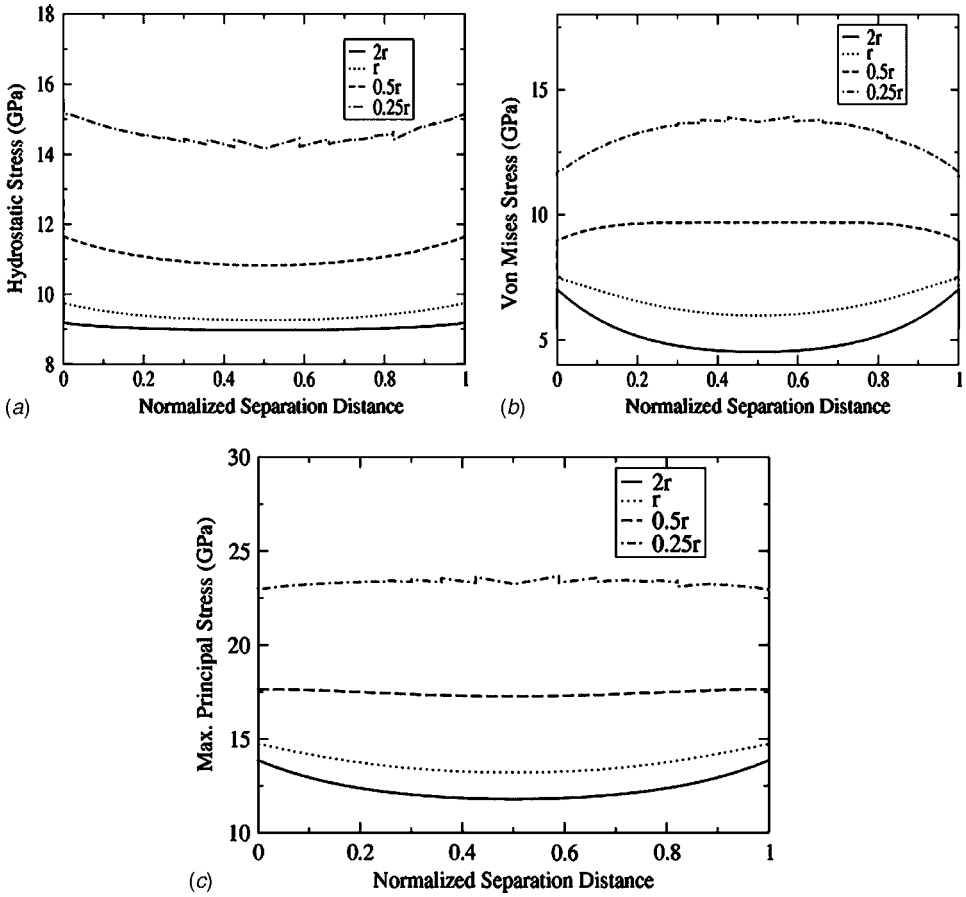

Fig. 6 Effect of fiber separation on the distribution of (*a*) hydrostatic stress; (*b*) Von Mises stress; and (*c*) maximum principal stress for an applied biaxial displacement corresponding to $\bar{\varepsilon}_{xx}=1$ and $\bar{\varepsilon}_{yy}=1$ and for a fiber radii, $r=1.75$ μm

$\bar{\varepsilon}_{yy}=3.2\text{e}-03$ are applied in the x and y-directions, respectively. In this case too, the debonding pattern is found to be equivalent for the 3D ABAQUS and the 2D VCFEM models and the stress distribution patterns are also in good agreement with one another.

Thus the results of the 3D model are in agreement with that of a 2D model for specific plane strain boundary value problems. The element has been checked for both a continuous interface and an interface defined by the bilinear cohesive law.

4 Effect of Relative Fiber Spacing and Volume Fraction on Matrix Stress

A two-fiber model of the steel-epoxy composite with unidirectional fibers is tested and the effect of the relative fiber spacing and volume fraction on the stress distribution pattern in the matrix is studied. As mentioned earlier, the only propagating mode of failure considered in the study is interfacial debonding. However, the distribution of the hydrostatic, Von Mises and the maximum principal stresses in the otherwise undamaged matrix are given for information. Again, the matrix has a potential failure mode due to cavitation and one due to a shearing mode, precipitated by the hydrostatic and Von Mises stresses, respectively. The maximum principal stress is reported since this component may affect the direction of growth of an initial cavitation. The critical region of study is the highly stressed matrix region lying between the two fibers.

We first consider different 3D realizations of the two-fiber model with equal radii such that the fibers are both aligned along the z-direction. For a given fiber volume fraction, the fiber spacing is varied and 3D models are constructed for analysis. The fiber volume fraction is then increased by increasing the fiber radii and another set of 3D models are created with varying the spacing between the fibers. One such representation is shown in Fig. 3(*a*). To impose plane strain conditions ($\varepsilon_{zz}=0$) on all the 3D, the front and back faces are constrained in the z-direction. The FEA boundary conditions include the bottom face and the left face being constrained in the y- and x-directions, respectively. Periodic boundary conditions are imposed such that the top face remains straight during deformation. A continuous interface is assumed between the fiber and matrix to study the stress states in the matrix prior to the onset of debonding. All the 3D models are subjected to two different sets of loading conditions, one with a uniaxial displacement applied in the positive x-direction, resulting in $\bar{\varepsilon}_{xx}=1$, and the other with a biaxial displacement, corresponding to $\bar{\varepsilon}_{xx}=1$ and $\bar{\varepsilon}_{yy}=1$ in the x and y directions, respectively.

Figures 5(*a*)–5(*c*) show the distribution of the hydrostatic, Von Mises and maximum principal stresses for different fiber spacing. The radii of the fibers in this case are 1.75 μm and the fiber volume fraction is 20%. The plots are obtained by computing the stress values along a line drawn parallel to the x-axis from points A to B as shown in Fig. 3(*a*). The plots are generated for the various fiber spacing for the given fiber radii and the distances are normalized in order to compare the stress distributions. For a given plot, the normalized distance at a given point in the line AB [Fig. 3(*a*)] is obtained by dividing the distance of that point from the point A with the total distance of separation AB and will have values ranging between 0 and 1, respectively. From Fig. 5(*a*), it is observed that the maximum value for the hydrostatic stresses occurs at the fiber matrix interface and the value tends to decrease slowly away from the interface. The same trend is observed irrespective of the fiber spacing. This is attributed to the high value of

σ_{yy} at the interface, resulting in higher values for the hydrostatic stress at the interface. The Von Mises stress [Fig. 5(*b*)] shows an opposite trend from that of the hydrostatic stress. The maximum value occurs away from the fiber matrix interface near the middle of the separation. The minimum value is observed at the interface for all the fiber spacings considered. In the case of maximum principal stresses, it is seen from Fig. 5(*c*) that for large fiber spacing, the maximum principal stress tends to have a small dip in its value at the middle of the separation. There is no noticeable change in the value of the maximum principal stress as the fibers approach each other.

The second set of results corresponds to the biaxial displacements applied in the *x* and *y*-directions. Figures 6(*a*)–6(*c*) show the distribution of the hydrostatic, Von Mises and maximum principal stresses for normalized separation distances considered for study for a fiber volume fraction of 20% and fiber radii of 1.75 μm. The hydrostatic stresses [Fig. 6(*a*)] are almost constant at larger spacing between the fibers. As the fibers come closer, there is a small dip in the hydrostatic stress values away from the interfaces near the middle of the separation. The maximum value is at the interface. The Von Mises stresses [Fig. 6(*b*)] show a decreasing trend in values away from the interfaces when there is a large distance of separation. But, as the fibers come close to each other, the maximum value of Von Mises stress is seen at the middle of the separation between the two fibers and the minimum value is at the fiber matrix interfaces. The maximum principal stresses [Fig. 6(*c*)] show the same trend as that of the uniaxial loading case by having a constant value for small spacing between the two fibers. For larger fiber spacing, there is a dip in the value away from the fiber matrix interfaces.

Another common observation in both the loading cases is that, as the spacing between the two fibers decreases, there is an increase in the magnitude of stresses. Also, there is no change in the stress distribution trend when there is an increase or decrease of fiber volume fraction. An increase or decrease in the fiber radii only results in a change in the magnitude of stresses and does not affect the distribution trend for quantities plotted. Figures 7(*a*) and 7(*b*) depict the distribution of hydrostatic and Von Mises stresses for one such case, where the relative fiber radii are 3 μm and the fiber volume fraction is 50%. The distribution in Figs. 7(*a*) and 7(*b*) for hydrostatic and Von Mises stresses depict the same trend as that of Figs. 5(*a*) and 5(*b*), and the variation is only in the magnitude of the stress values. It should be noted that the observations for the specific boundary value problems considered here may not be true in general.

5 Effects of Fiber Orientation on Debonding Initiation and Progression

This section is aimed at studying the effects of local fiber misalignment and orientation on the initiation and propagation of damage due to interfacial debonding in a two-fiber 3D composite model. The problems considered give an idea of local behavior due to the interaction between fibers in the composite microstructure. Initially, a two-fiber 3D composite model with fibers of equal radii is considered for study and the following metrics are used to quantify the effects of fiber orientations on the nature of interfacial damage.

5.1 Macroscopic Stress–Strain Behavior. The definitions of the macroscopic stresses and strains are given in Sec. 3 of this paper. For a specified boundary value problem, the macroscopic stress–strain plots are computed for different fiber orientations and compared against each other. It is of significance to see if the macroscopic stress–strain plots can differentiate the various orientations modeled at the microstructural level.

5.2 Macroscopic Stress–Strain for Debonding Initiation. This is defined as the externally applied value of the macroscopic stresses and strains at which debonding initiates at the interface.

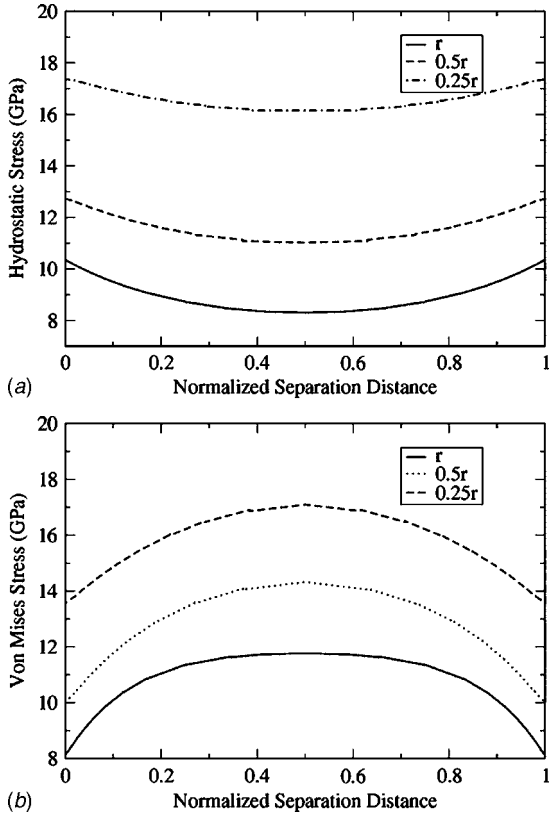

Fig. 7 Effect of fiber separation on the distribution of (*a*) hydrostatic stress; (*b*) Von Mises stress for an applied uniaxial displacement corresponding to $\bar{\varepsilon}_{xx}=1$ for a fiber radii, $r=3$ μm

5.3 Fraction of Damaged Interface. The fraction of the damaged interface is defined as the ratio of the area of the interface that is damaged to the total interface area. The ratio can be evaluated for different fiber orientations and compared against one another.

Some of these metrics may be susceptible to experimental observation. In conjunction with the modeling results, this can lead to further understanding of these complex failure mechanisms and their impact on composite behavior. The parameters defined above are used in quantifying the damage for three different fiber orientation scenarios involving the two-fiber model. In the first case, one end of each of the fibers is placed on the *x*-axis and the fibers are oriented in the *xz* plane as shown in Fig. 8(*a*). Figure 8(*b*) shows the top view of the 3D model showing the angle of orientation (θ°) between the two fibers. Different realizations of this case are generated by varying this orientation angle. The fiber volume fraction for the first case is kept at 20% and the fiber radii are 1.75 μm in each case. The block dimensions of the model shown in Fig. 8 are 14 μm$\times$7 μm$\times$7 μm, respectively. In the second case, the fiber ends are placed on the *y*-axis and oriented parallel to the *xz* plane as shown in Fig. 9(*b*). The corresponding top view of the two-fiber model showing the angle of orientation (θ°) between the fibers is depicted in Fig. 9(*a*). By varying the orientation angle, θ°, different 3D models are generated such that the fiber volume fraction for all the models is kept at 10%. The high degree of fiber orientation, coupled with a certain minimum distance considered between the fiber surface and the boundary of the model, impose a restriction on the fiber volume fraction of these models (10%) being less than the first set of models (20%). The fiber radii for all the models have a value of 1.75 μm and the *y*-distance between the two fiber centers is 7 μm. The block dimensions of the model shown in Fig. 9 are 14 μm$\times$14 μm $\times$7 μm, respectively. The third case differs from the second case

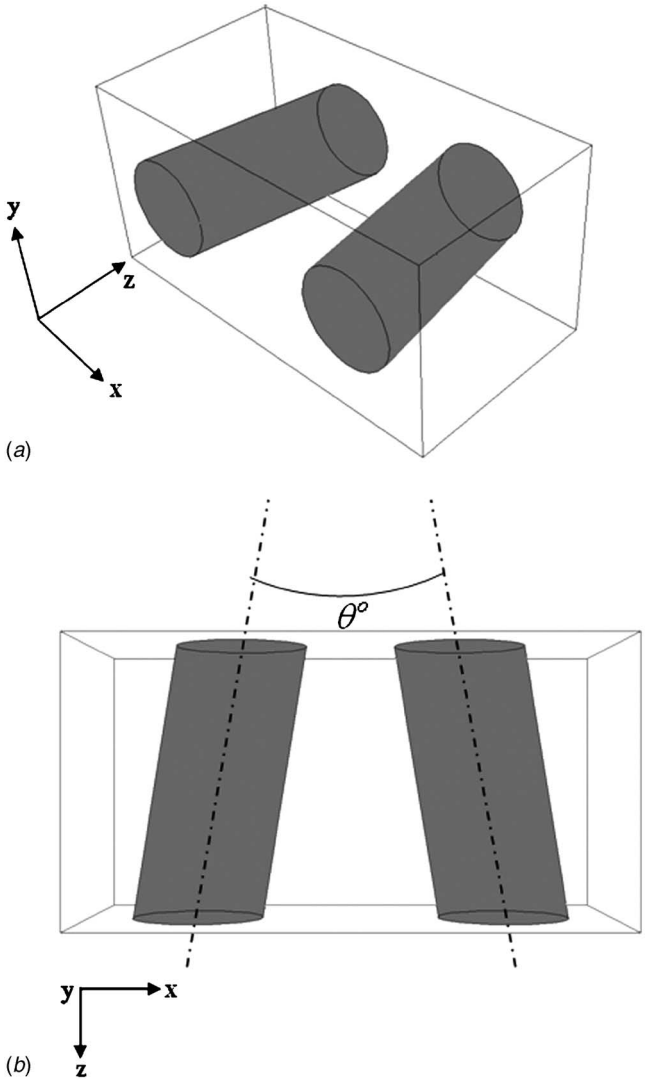

Fig. 8 (*a*) Three-dimensional two-fiber RVE with fibers placed alongside each other and oriented with respect to one another; (*b*) top view of the RVE defining the fiber orientation and the orientation angle $\theta°$

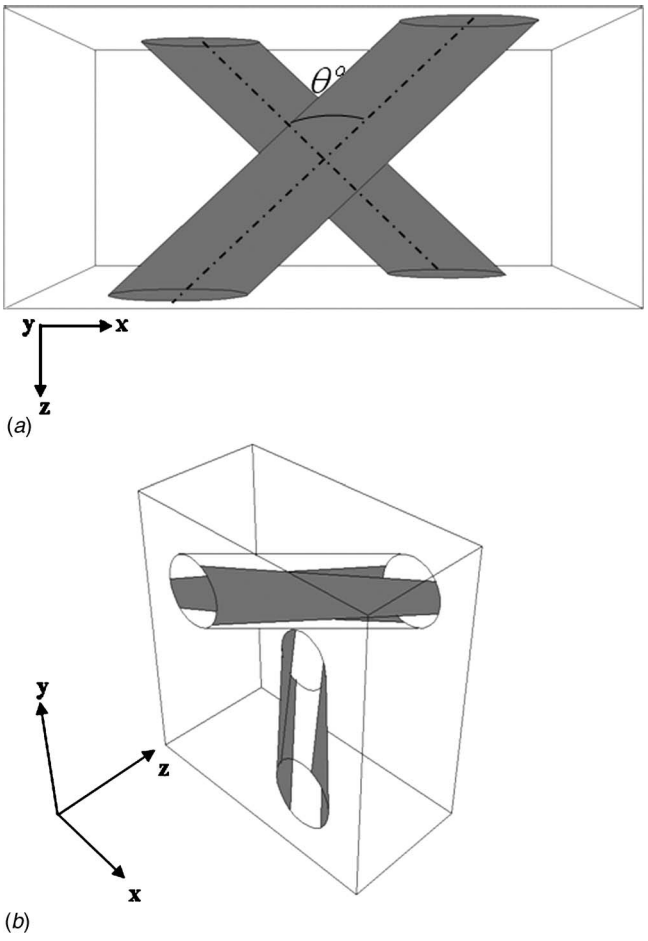

Fig. 9 Two-fiber RVE with one fiber placed above the other fiber and oriented with respect to each other: (*a*) top view defining the fiber orientation and the angle $\theta°$; (*b*) gray-shaded region of interfacial debonding at the end of loading

in that, for a specified angle of orientation, $\theta°$, the fibers are moved towards each other along the y-axis. The fiber volume fraction and radii are the same as that of the previous case. For all the 3D models, the FEA boundary conditions consist of the three faces lying in the yz plane, xz plane, and xy plane to be constrained in the x, y, and z-directions, respectively. A uniaxial displacement that corresponds to $\bar{\varepsilon}_{xx}=3.0\text{e}-03$ is applied along the x-direction to the face perpendicular to the x-axis. The displacement is applied in small equal increments. Additional boundary conditions are imposed on the other two free faces so that the edges remain straight during deformation. The properties of the materials and the cohesive zone parameters used in the analysis are as defined in Sec. 3 of the paper. The damage occurs at the inside of these two–fiber models, at the fiber-matrix interfaces. For a given integration point, damage is said to have occurred when the displacement jump, δ exceeds the δ_e value of the cohesive zone model (i.e., at complete debonding). The displacement jump, δ is determined at each of the integration points and by comparing these values against the δ_e value, the debonding locations at the interface can be recorded. Figure 9(*b*) shows the debonding response of a two-fiber model with an angle of orientation of 52 deg, subjected to load and boundary conditions stated above. The grey-shaded regions in the figure represent areas of the fiber–matrix interface that have undergone debonding. An uneven nature of debonding progression on either side of the fiber is observed in Fig. 9(*b*).

Figures 10(*a*)–10(*c*) depict the effect of the fiber orientation as defined by Fig. 8(*b*) on the metrics considered to represent the interfacial damage only. As mentioned earlier, no cavitation or shear failure is assumed in matrix. From Fig. 10(*a*), it is observed that the macroscopic stress–strain plots show the same trend for the increasing angles of orientation and there is negligible difference between the plots. Hence, the macroscopic plot may not be able to distinguish varied fiber orientations within a specified fiber volume fraction. The variation of macroscopic strain, $\bar{\varepsilon}_{xx}$ for damage initiation with the orientation angle is shown in Fig. 10(*b*). Though the strain values lie within a narrow range, the macroscopic strain required for damage to initiate decreases with the increase in the orientation angle. This means that a misalignment of fibers in the matrix, under the present boundary conditions, can quicken the initiation of the damage due to interfacial debonding. Figure 10(*c*) compares the fraction of damaged interface for various orientation angles. It is seen that the fraction of damaged area is minimum for fibers aligned parallel with each other. The area tends to increase with increase in the orientation angle. There is a sharp jump in the rate of interfacial damage when the orientation angle increases from 5 deg to 10 deg.

Figures 11(*a*)–11(*c*) show the effect of the fiber orientation as defined by Figure 9(*a*) on the parameters used to represent the interfacial damage. In this case also, the macroscopic stress–strain

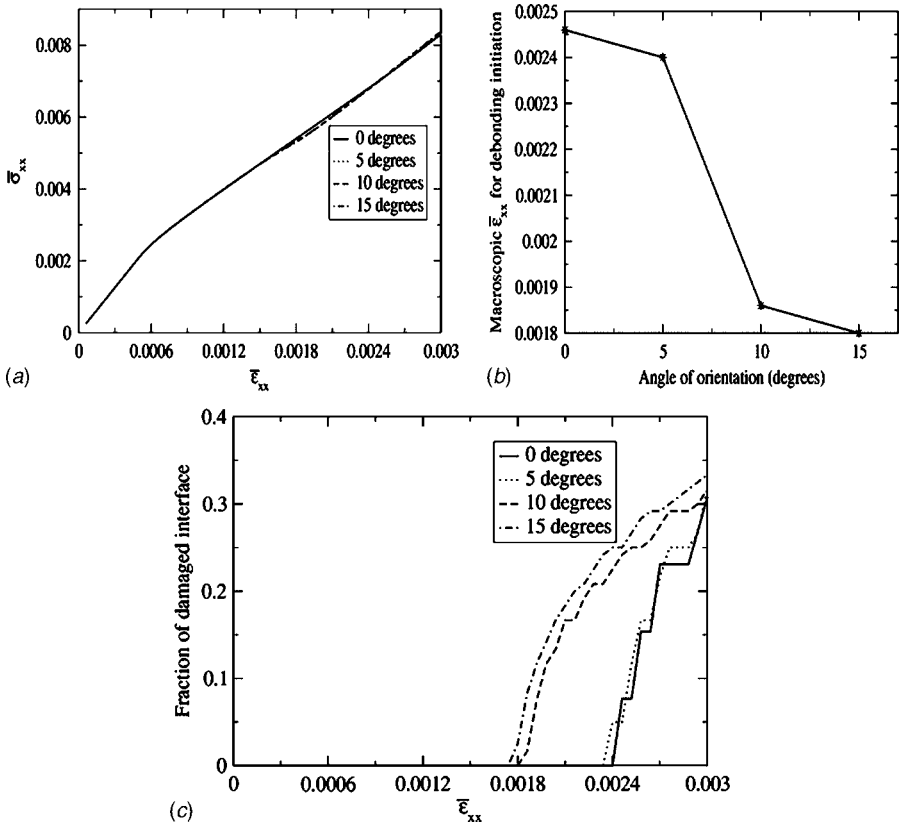

Fig. 10 Effect of fiber orientation on (*a*) macroscopic stress–strain ($\bar{\varepsilon}_{xx}$–$\bar{\sigma}_{xx}$) plots for applied $\bar{\varepsilon}_{xx}$=3.0e−03; (*b*) macroscopic strain, $\bar{\varepsilon}_{xx}$ for debonding initiation; (*c*) fraction of damaged interface

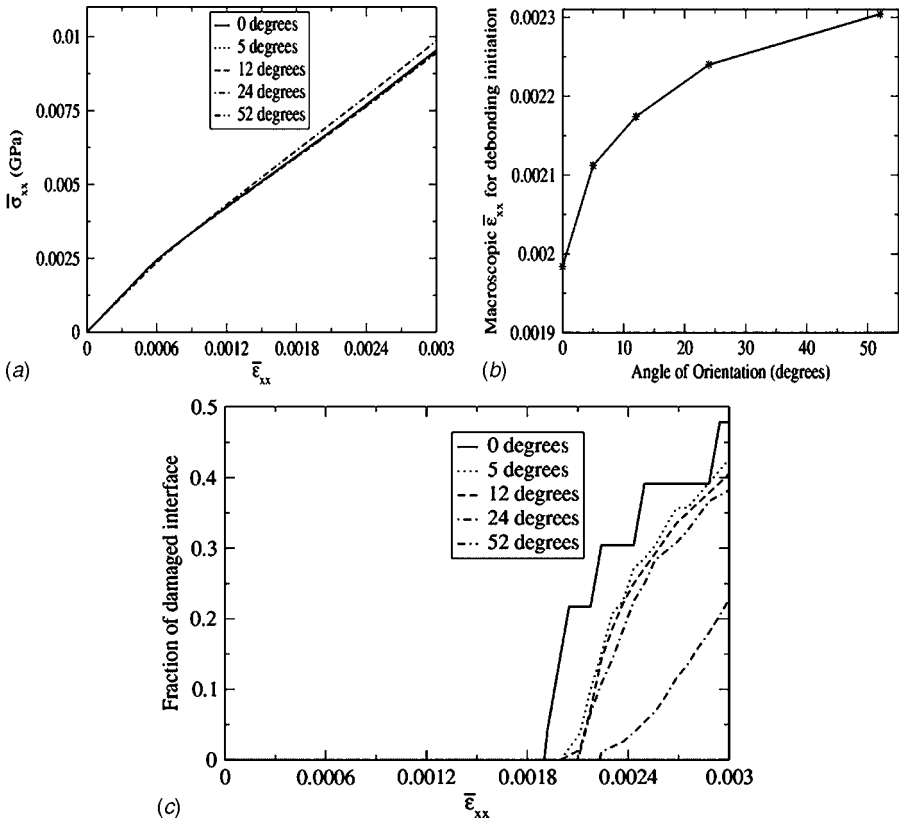

Fig. 11 Effect of fiber orientation on (*a*) macroscopic stress–strain ($\bar{\varepsilon}_{xx}$–$\bar{\sigma}_{xx}$) plots for applied $\bar{\varepsilon}_{xx}$=3.0e−03; (*b*) macroscopic strain, $\bar{\varepsilon}_{xx}$ for debonding initiation; (*c*) fraction of damaged interface

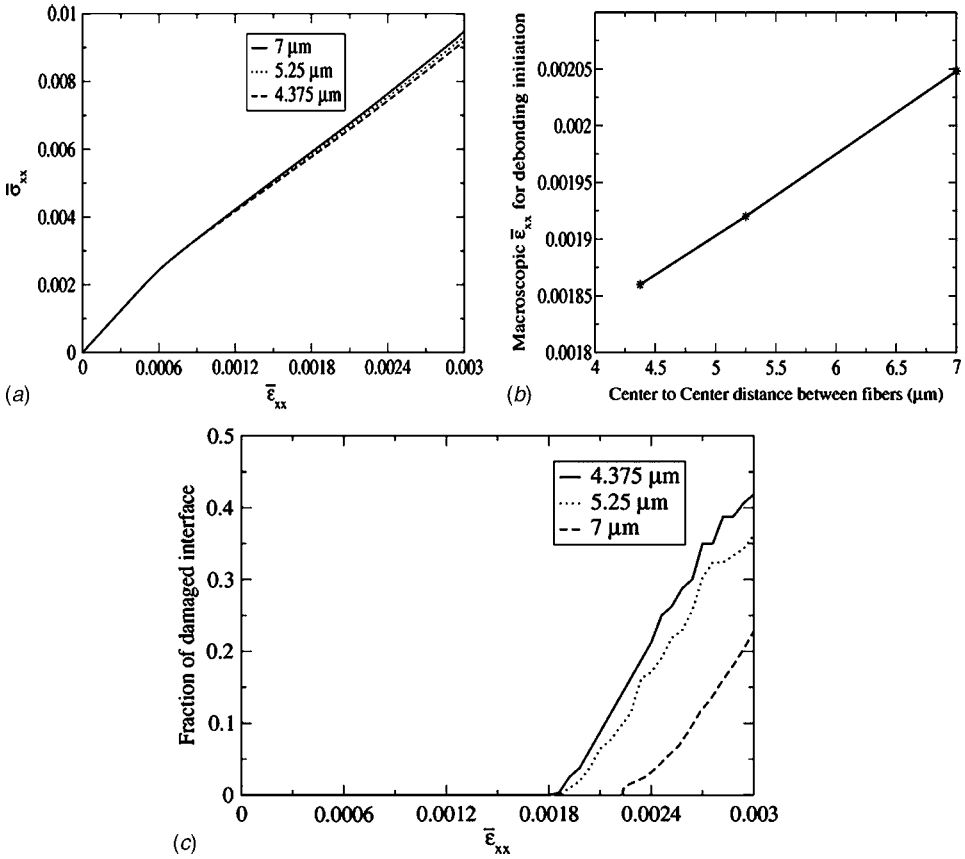

Fig. 12 Effect of the center to center distance between fibers on (*a*) macroscopic stress–strain ($\bar{\varepsilon}_{xx}-\bar{\sigma}_{xx}$) plots for applied $\bar{\varepsilon}_{xx}$=3.0e−03; (*b*) macroscopic strain, $\bar{\varepsilon}_{xx}$ for debonding initiation; (*c*) fraction of damaged interface, for a specified orientation angle of 48 deg

plots [Fig. 11(*a*)] show the same trend for the increasing angles of orientation and there is little difference between the plots. Figure 11(*b*) depicts the variation of macroscopic strain, $\bar{\varepsilon}_{xx}$ for damage initiation with the orientation angle. The trend in this case is opposite to that of the previous case. With an increase in the orientation angle, the strain required for debonding to initiate increases. This means that the misalignment of the fibers may prove to be advantageous as the onset of damage is delayed. The comparison of the fraction of damaged area for the various fiber orientations with increasing strain is depicted in Fig. 11(*c*). In this case, the rate of interfacial damage is highest for fibers placed one above the other and aligned parallel with each other. With increase in orientation angle, the fraction of interfacial damage reduces and has the minimum value for the highest orientation angle considered (52 deg).

Extending the study using the second definition of the orientation angle, a fixed angle of 48 deg as defined by Fig. 9 is specified between the fibers. The fibers are brought closer by decreasing the center to center distance along the *y*-axis and the metrics for damage quantification are computed. This data is shown in Fig. 12. The macroscopic stress–strain curves [Fig. 12(*a*)] for the three center to center distances considered do not show any variation and they depict the same trend. The macroscopic strain required for damage initiation reduces when the fibers are brought close together as shown in Fig. 12(*b*). The fraction of damaged interface [Fig. 12(*c*)] also depicts an increase when they are brought close together. This means that though misalignment may result in delayed damage initiation and reduced interfacial damage, the distance of separation between the fibers also plays a crucial role in triggering the onset of damage.

6 Conclusions

A 3D cohesive interface element is developed in ABAQUS in this paper to simulate damage due to interfacial debonding in composite microstructures. The element is made of 16 nodes with a quadratic interpolation. The 3D element is validated by comparing with the results of 2D VCFEM for selected boundary value problems. The element is then used to model the fiber–matrix interface for a two fiber 3D microstructure and the evolution of damage due to interfacial debonding is analyzed. The effect of the relative fiber spacing and volume fraction on the matrix stress distribution pattern is studied for selected problems. Not surprisingly, the fiber spacing plays an important role in the stress distribution pattern in the matrix. The study examines the likely regions of failure initiation with the consideration of debonding mode alone. If the two fibers are parallel and a J_1 failure criterion is assumed, failure will initiate at the fiber matrix interface, while a failure criterion based on the Von Mises stress would indicate initiation of a shear mode of failure in the matrix region midway between the two fibers.

A study to understand the effect of the fiber orientation on the initiation and progression of interfacial debonding is also done with a 3D two-fiber model. The damage is quantified using a set of metrics that included the macroscopic stress–strain plot, macroscopic strain for damage initiation and the fraction of damaged interface area. The macroscopic stress–strain plot may not be able to distinguish different fiber orientations for a specific fiber volume fraction. All of these studies assume particular constituent properties and neglect matrix-only failures. The study also shows the potential effects of fiber orientation and spacing. Two different

architectures are considered—fibers in the same plane and parallel planes—and in the former case, the parallel arrangement is found to be the most effective in delaying debonding initiation and also the area of interface damaged is found to be a minimum. However, for the latter architecture, an increase in orientation angle results in significant slowdown of damage initiation and propagation. This means that certain combinations of spacing and alignment of fibers in composite layers may delay the onset of damage due to interfacial debonding than a regular unidirectional arrangement. Similar models can be used to assess effects of misalignment error and the corresponding need to control microstructural morphology.

All of the inferences regarding failure modes are based upon the prescribed boundary conditions employed in this study and only consider the interaction effect of two fibers, rather than the multitude that could occur in a practical composite. We have also assumed that debonding is the only propagating failure mode. However, the trends observed and analysis technique employed can be valuable for more exhaustive studies of the effects of fiber spacing and misalignment.

Acknowledgment

This work has been supported by the Air Force Office of Scientific Research through Grant No. F49620-98-1-01-93 (Program Director: Dr. B. L. Lee). This sponsorship is gratefully acknowledged. S.S. and S.G. also gratefully acknowledge the support of this work by Dr. Greg Schoeppner of the Air Force Research Laboratory through additional funding. Computer support by the Ohio Supercomputer Center through Grant No. PAS813-2 is also acknowledged.

References

[1] Benveniste, Y., 1984, "On the Effect of Debonding on the Overall Behavior of Composite Materials," Mech. Mater., **3**, pp. 349–358.
[2] Hashin, Z., 1990, "Thermoelastic Properties of Fiber Composites with Imperfect Interface," Mech. Mater., **8**, pp. 333–348.
[3] Pagano, N. J., and Tandon, G. P., 1990, "Modeling of Imperfect Bonding in Fiber Reinforced Brittle Matrix Composites," Mech. Mater., **9**, pp. 49–64.
[4] Yuan, F. G., Pagano, N. J., and Cai, X., 1997, "Elastic Moduli of Brittle Matrix Composites with Interfacial Debonding," Int. J. Solids Struct., **34**, pp. 177–201.
[5] Needleman, A., 1987, "A Continuum Model for Void Nucleation by Interfacial Debonding," J. Appl. Mech., **54**, pp. 525–531.
[6] Needleman, A., 1990, "An Analysis of Decohesion Along an Imperfect Interface," Int. J. Fract., **42**, pp. 21–40.
[7] Needleman, A., 1992, "Micromechanical Modeling of Interfacial Decohesion," Ultramicroscopy, **40**, pp. 203–214.
[8] Tvergaard, V., 1990, "Effect of Fiber Debonding in a Whisker-Reinforced Metal," Mater. Sci. Eng., A, **125**, pp. 203–213.
[9] Tvergaard, V., 1995, "Fiber Debonding and Breakage in a Whisker Reinforced Metal," Mater. Sci. Eng., A, **190**, pp. 215–222.
[10] Ghosh, S., Ling, Y., Majumdar, B. S., and Kim, R., 2000, "Interfacial Debonding in Multiple Fiber-Reinforced Composites," Mech. Mater., **32**, pp. 561–591.
[11] Li, Shanhu, and Ghosh, S., 2004, "Debonding in Composite Microstructures with Morphological Variations," Int. J. Comput. Math., **1**, pp. 121–149.
[12] Foulk, J. W., Allen, D. H., and Helms, K. L. E., 2000, "Formulation of a Three-Dimensional Cohesive Zone Model for Application to a Finite Element Algorithm," Comput. Methods Appl. Mech. Eng., **183**, pp. 51–66.
[13] Allen, D. H., Jones, R. H., and Boyd, J. G., 1994, "Micro-Mechanical Analysis of Continuous Fiber Metal Matrix Composite Including the Effects of Matrix Visco-Plasticity and Evolving Damage," J. Mech. Phys. Solids, **42**, pp. 502–529.
[14] Lo, D. C., and Allen, D. H., 1994, "Modeling of Delamination Damage Evolution on Laminated Composites Subjected to low Velocity Impact," Int. J. Damage Mech., **3**, pp. 378–407.
[15] Lissenden, C. J., and Herakovich, C. T., 1995, "Numerical Modeling of Damage Development and Viscoplasticity in Metal Matrix Composites," Comput. Methods Appl. Mech. Eng., **126**, pp. 289–303.
[16] Geubelle, P. H., 1995, "Finite Deformation Effects in Homogeneous and Interfacial Fracture," Int. J. Solids Struct., **32**, pp. 1003–1016.
[17] Camacho, G. T., and Ortiz, M., 1996, "Computational Modeling of Impact Damage in Brittle Materials," Int. J. Solids Struct., **33**, pp. 2899–2938.
[18] Ortiz, M., and Pandolfi, A., 1999, "Finite-Deformation Irreversible Cohesive Element for Three-Dimensional Crack-Propagation Analysis," Int. J. Numer. Methods Eng., **44**, pp. 1267–1282.
[19] Scheider, Ingo, 2001, "Cohesive Model for Crack Propagation Analyses of Structures with Elastic-Plastic Material Behavior: Foundations and Implementation," GKSS Research Center, Geesthacht.
[20] Segurado, Javier, and LLorca, Javier, 2004, "A New Three-Dimensional Interface Finite Element to Simulate Fracture in Composites," Int. J. Solids Struct., **41**, pp. 2977–2993.
[21] Abaqus, 2001, "User's Manual," Hibbit, Karlsson, and Sorensen, Inc.
[22] Moorthy, S., and Ghosh, S., 2000, "Adaptivity and Convergence in the Voronoi Cell Finite Element Model for Analyzing Heterogeneous Materials," Comput. Methods Appl. Mech. Eng., **185**, pp. 37–74.
[23] Raghavan, P. and Ghosh, S., 2004, "Concurrent Multi-Scale Analysis of Elastic Composites by a Multi-Level Computational Model," Comput. Methods Appl. Mech. Eng., **193**, pp. 497–538.
[24] Moorthy, S., and Ghosh, S., 1996, "A Model for Analysis of Arbitrary Composite and Porous Microstructures with Voronoi Cell Finite Elements," Int. J. Numer. Methods Eng., **39**, pp. 2363–2398.
[25] Chandra, N., Li, H., Seth, C., and Ghonem, H., 2002, "Some Issues in the Application of Cohesive Zone Models for Metal Ceramic Interfaces," Int. J. Solids Struct., **39**, pp. 2827–2855.
[26] Raghavan, P., and Ghosh, S., "A Continuum Damage Mechanics Model for Unidirectional Composites Undergoing Interfacial Debonding," Mech. Mater. (in press).
[27] Raghavan, P., and Ghosh, S., 2004, "Adaptive Multi-Scale Computational Modeling of Composite Materials," Comput. Model. Eng. Sci., **5**, pp. 151–170.